

Frequency division multiplexing readout of a transition edge sensor bolometer array with microstrip-type electrical bias lines

Wang, Q.; Khosropanah, P.; Van Der Kuur, J.; De Lange, G.; Audley, M. D.; Aminaei, A.; Ilyas, S.; Van Der Tak, F.; Gao, J. R.

DOI

[10.1063/5.0108786](https://doi.org/10.1063/5.0108786)

Publication date

2022

Document Version

Final published version

Published in

Review of Scientific Instruments

Citation (APA)

Wang, Q., Khosropanah, P., Van Der Kuur, J., De Lange, G., Audley, M. D., Aminaei, A., Ilyas, S., Van Der Tak, F., & Gao, J. R. (2022). Frequency division multiplexing readout of a transition edge sensor bolometer array with microstrip-type electrical bias lines. *Review of Scientific Instruments*, 93(12), Article 124901. <https://doi.org/10.1063/5.0108786>

Important note

To cite this publication, please use the final published version (if applicable).
Please check the document version above.

Copyright

Other than for strictly personal use, it is not permitted to download, forward or distribute the text or part of it, without the consent of the author(s) and/or copyright holder(s), unless the work is under an open content license such as Creative Commons.

Takedown policy

Please contact us and provide details if you believe this document breaches copyrights.
We will remove access to the work immediately and investigate your claim.

Green Open Access added to TU Delft Institutional Repository

'You share, we take care!' - Taverne project

<https://www.openaccess.nl/en/you-share-we-take-care>

Otherwise as indicated in the copyright section: the publisher is the copyright holder of this work and the author uses the Dutch legislation to make this work public.

Frequency division multiplexing readout of a transition edge sensor bolometer array with microstrip-type electrical bias lines

Cite as: Rev. Sci. Instrum. **93**, 124901 (2022); <https://doi.org/10.1063/5.0108786>

Submitted: 10 July 2022 • Accepted: 26 November 2022 • Published Online: 20 December 2022

 Q. Wang, P. Khosropanah, J. van der Kuur, et al.



View Online



Export Citation



CrossMark

ARTICLES YOU MAY BE INTERESTED IN

[Precise pulsed magnetic field mapping using a compact pick-up probe for a pulsed sextupole magnet](#)




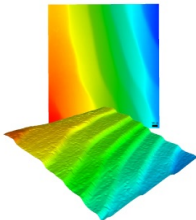
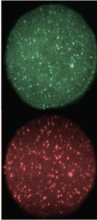
Review of Scientific Instruments **93**, 123306 (2022); <https://doi.org/10.1063/5.0111979>

[Development of multichord ion Doppler spectroscopy system for toroidal flow measurement of field-reversed configuration](#)

Review of Scientific Instruments **93**, 123512 (2022); <https://doi.org/10.1063/5.0101878>

[Development of a high-power pulse-forming network Marx generator with a long pulse duration](#)

Review of Scientific Instruments **93**, 124704 (2022); <https://doi.org/10.1063/5.0124394>

 MCL MAD CITY LABS INC. www.madcitylabs.com	<p>Nanopositioning Systems</p> 	<p>Modular Motion Control</p> 	<p>AFM and NSOM Instruments</p> 	<p>Single Molecule Microscopes</p> 
-----------------------------------------------------------------------------------------------------------------------------------------------------------------------------------------	--------------------------------------------------------------------------------------------------------------------	--------------------------------------------------------------------------------------------------------------------	-----------------------------------------------------------------------------------------------------------------------	--------------------------------------------------------------------------------------------------------------------------

Frequency division multiplexing readout of a transition edge sensor bolometer array with microstrip-type electrical bias lines

Cite as: Rev. Sci. Instrum. 93, 124901 (2022); doi: 10.1063/5.0108786

Submitted: 10 July 2022 • Accepted: 26 November 2022 •

Published Online: 20 December 2022



View Online



Export Citation



CrossMark

Q. Wang,^{1,2}  P. Khosropanah,¹ J. van der Kuur,¹ G. de Lange,¹  M. D. Audley,¹ A. Aminaei,¹ S. Ilyas,¹ M. L. Ridder,¹  A. J. van der Linden,¹  M. P. Bruijn,¹  F. van der Tak,^{1,2}  and J. R. Gao^{1,3,a)} 

AFFILIATIONS

¹SRON Netherlands Institute for Space Research, Landleven 12, 9747 AD Groningen and Niels Bohrweg 4, 2333 CA Leiden, The Netherlands

²Kapteyn Astronomical Institute, University of Groningen, 9747 AD Groningen, The Netherlands

³Optics Group, Department of Imaging Physics, Delft University of Technology, 2628 CJ Delft, The Netherlands

^{a)}Author to whom correspondence should be addressed: J.R.Gao@sron.nl

ABSTRACT

We demonstrate multiplexed readout of 43 transition edge sensor (TES) bolometers operating at 90 mK using a frequency division multiplexing (FDM) readout chain with bias frequencies ranging from 1 to 3.5 MHz and a typical frequency spacing of 32 kHz. We improve the previously reported performance of our FDM system by two important steps. First, we replace the coplanar wires with microstrip wires, which minimize the cross talk from mutual inductance. From the measured electrical cross talk (ECT) map, the ECT of all pixels is carrier leakage dominated. Only five pixels show an ECT level higher than 1%. Second, we reduce the thermal response speed of the TES detectors by a factor of 20 by increasing the heat capacity of the TES, which allows us to bias all TES detectors below 50% in transition without oscillations. We compare the current–voltage curves and noise spectra of the TESs measured in single-pixel mode and multiplexing mode. We also compare the noise equivalent power (NEP) and the saturation power of the bolometers in both modes, where 38 pixels show less than 10% difference in NEP and 5% difference in saturation power when measured in the two different modes. The measured noise spectrum is in good agreement with the simulated noise based on measured parameters from an impedance measurement, confirming that our TES is dominated by phonon noise.

Published under an exclusive license by AIP Publishing. <https://doi.org/10.1063/5.0108786>

I. INTRODUCTION

Transition edge sensor (TES) bolometer arrays are important for the next generation of far-infrared (FIR) space observatories.^{1,2} Multiplexing techniques are essential for reading out TES arrays due to the fact that they can decrease the number of cold electrical wires, thus minimizing the heat load on the cold stage.^{2,3} Frequency division multiplexing (FDM) is one of the most promising techniques for the readout of TES bolometer arrays.^{3,4} In an FDM readout system, each detector is in series with a specific LC (inductor-capacitor) filter, and an array of TESs is AC voltage biased with a comb of frequencies at the resonance frequencies of those LC-filters, typically within a bandwidth of a few MHz.^{4,5} The resulting comb of

currents is measured by a superconducting quantum interference device (SQUID) and amplified by the rest of the readout chain. To increase the number of detectors per SQUID, a digitally generated nulling feedback signal is applied to the SQUID.⁶ Limited by the speed of the feedback electronics, one readout chain can maximally accommodate on the order of 100 pixels. The maximum number of pixels that can be read out by one chain is called the multiplexing factor. Thus, dozens of such readout chains must operate in parallel to read out a large array of 10^3 – 10^4 detectors. Compared to other promising readout techniques such as time division multiplexing (TDM)^{7–9} and microwave-SQUID readout,^{10–12} the FDM readout techniques demonstrate a competitive performance.^{13,14} In addition, the power dissipation in an FDM system is almost zero on

the mK stage due to the passive readout elements in the FDM system since the dissipation of the first-stage SQUID is usually within a few nW.

Over the past decade, several FDM readout systems for TES arrays have been developed for ground-based observatories, such as the APEX-SZ,¹⁵ the SPT-3G,¹⁶ and the POLARBEAR.¹⁷ The state of the art of FDM technology in ground-based applications is reported in Ref. 16, where 206 pixels were successfully read out with six SQUID amplifiers, leading to a multiplexing factor of 35. Furthermore, this FDM system has a relatively large frequency spacing, which varies from about 40 kHz at the low-frequency end (≤ 2 MHz) to over 60 kHz at the high-frequency range (≥ 3 MHz). The FDM readout technique was successfully applied for the balloon-borne mission EBEX^{18,19} and is currently being developed for the balloon-borne explorer LSPE.^{20,21} Both have a multiplexing factor of 16. The FDM readout technique is also considered for space observatories, such as the LiteBird^{22,23} and the far-infrared instrument (SAFARI) on board of the SPICA.^{24,25} Compared to ground-based instruments, spacecraft platforms usually have limited resources of power, mass, and volume.^{24,26} Those requirements could restrict the use of the heritage of ground-based FDM technology. The requirements of SPICA/SAFARI, for example, not only impose a different configuration of the FDM readout chain than that of ground-based systems but also require different LC filter designs, e.g., a small frequency spacing and a compact chip design.²⁷ Up until now, there has been no reported FDM readout system that has been flown in space.

Our previous work demonstrated an FDM system that has successfully read out 60 low-noise TES bolometers.¹⁴ However, the cross talk between pixels connected by coplanar wires in the same bundle of wires, which are closely and parallelly packed, is very high (more than 10%) due to their mutual inductance. High cross talk induces a large bias current leakage, which causes electrothermal instability and a high current noise level as well. Also, some pixels cannot be biased lower than 70% in transition, where annoying oscillations occur. When those pixels are biased lower in transition, their effective thermal response speed is too fast and is comparable with the electrical response speed. This initiates the oscillations, which lead to the unstable biasing of TES bolometers. Furthermore, the noise spectra show some excess noise. To reduce the cross talk, we have designed and fabricated a new TES array where microstrip-structured wires instead of coplanar wires are used to connect all the TES and where the thermal response time of the TES detectors is increased by augmenting their heat capacity. We apply a microstrip (line) as a pair of electrical bias lines to connect a TES to two bonding pads on the array chip. The microstrip consists of a superconducting Nb conductor separated from an Nb ground plane by a dielectric SiO₂ layer. The top Nb line is 3 μm in width, while the ground plane is 5 μm in width, both of which are 100 nm in thickness. The SiO₂ layer is 250 nm thick. The separation distance between two microstrips (center to center) varies and is typically 320 μm . However, they become closer around TESs, with a separation distance of 10 μm within a length of about 80 μm . The increase in heat capacity was realized by adding an Au layer structure instead of the Ta absorber in our previous TESs.¹⁴ The Au layer will not absorb any FIR radiation and thus can also mitigate the effect of possible stray light in our dedicated electrical characterization measurements. We do not expect our TES without the absorber to respond or absorb

submm and FIR optical signals. This was indirectly confirmed in our lab using an extremely low noise equivalent power (NEP) TES without the absorber, where the TES did not clearly show photon noise, although the presence of the stray light was expected.²⁸

In this paper, we report an FDM demonstration experiment in which 43 TES bolometers were simultaneously read out. We mapped the electrical cross talk (ECT) level of all 43 TES detectors using our FDM system, with all the detectors biased at their nominal operating point on the transition. The ECT level is dominated by carriers with less than 1% leakage from neighboring pixels, while the other pixels show a level less than 0.1%. We have successfully slowed the TES response by a factor of 20, which enables us to bias all the pixels lower than 50% in transition without any unwanted oscillations. Also, we find the measured noise spectra match well with those expected from phonon noise because no absorber is present in the TES bolometers.

II. EXPERIMENTAL SETUP

Figure 1(a) shows the TES array, LC filters, and first-stage SQUID used in our FDM demonstration. A zoomed photo of a TES bolometer from the array is shown in Fig. 1(b). A square Au layer is introduced to increase the heat capacity and thus slow down the response speed of the detector. There is no absorber in the bolometers, so our detector is in principle insensitive to any submm and far-infrared light. Therefore, our TES bolometer will not suffer from stray light as suggested in the previous study,¹⁴ and the noise will be dominated by phonon noise or other excess noise (if significant). Figure 1(c) shows the decoupled second-stage SQUID from VTT Technical Research Center of Finland Ltd. (VTT), which is located in the same copper sample enclosure as the TES array. The decoupled two-stage SQUID amplifier²⁹ decreases the readout noise, minimizes the common inductance that is due to the inductive coupling of the SQUID, and eliminates the back-action effect. The latter

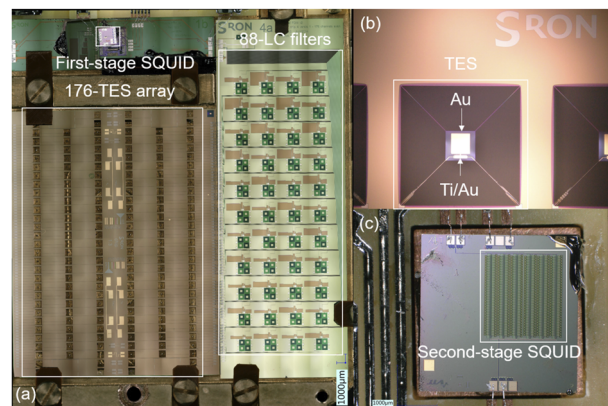


FIG. 1. (a) Photo of the 176-pixel TES array and an 88-LC filter chip, half of the TES array and 88-LC filters being connected via wire bonding. The first-stage SQUID is shown on top. (b) A zoomed photo of one TES pixel, which contains an Au structure to increase heat capacity. There are some unintended structures left on some of the Si₃N₄ legs, which might potentially introduce non-uniformity to the thermal conductance. (c) A photo of the second-stage SQUID, which is formed by hundreds of SQUIDs in series.

refers to a phenomenon where feedback noise is added to the input signal.¹⁴ The power dissipation of the first-stage SQUID and the second-stage SQUID is 2 and 750 nW, respectively. For this particular experiment, the high dissipation power of the second-stage SQUID is not a concern. However, for a space application, it will be arranged to 4 K stage, where there will usually be sufficient cooling power. Microstrip wires are used between each TES detector and the bonding pad to decrease mutual inductance in comparison with the coplanar wires that are very close to each other in our previous array.³⁰ Aluminum bonding wires are applied to connect the TES chip with the LC filter chip and become superconducting at our operating temperature. An adiabatic demagnetization refrigerator (ADR)³⁰ is used to cool down the bracket. Our measurements were performed at 90 mK, and the background magnetic field of the TES was nulled with a coil. Due to the instability of the cooling power and the presence of 50 Hz noise, we observed a measurement error of 5% in the current–voltage (IV) curve and 10% in the noise spectrum, respectively.¹⁴

Although we could reach a high multiplexing factor of up to 176 if we connected the whole TES array, the ECT level would be a factor of 4 higher than in the case when only half of the TES array is connected. Therefore, to simplify the experiment, we chose to connect only half of the TES array to one of the LC filter chips (with 88 resonators) with resonance frequencies ranging from 1 to 3.5 MHz and a frequency spacing of 32 ± 4 kHz. After performing an initial network analyzer scan (NWA) via an AC bias line from 1 to 3.5 MHz, we found 70 LC filters with a high quality factor ($\geq 10^4$), among the connected 88 resonators. However, because the yield of this specific TES array is relatively low, likely due to the deposition of an additional Au layer, eventually only 43 TES pixels with relatively sharp transitions together with their corresponding LC filters are chosen for our FDM experiment. The relation between pixel number and resonance frequency is shown in Fig. 2(a). Pixel 1 corresponds to

the lowest frequency of 1 MHz, while pixel 43 corresponds to the highest frequency of 3.5 MHz in this case. To find the precise resonance frequency, we perform a fine current scan (with feedback on) within a 200 Hz bandwidth around the resonance frequency estimated from the NWA scan while the TES devices are in their superconducting state. Then, by fitting the measured data, the Q factor of this pixel can be calculated according to $Q = f_0/\Delta f$, where f_0 is the resonance frequency and Δf is the frequency bandwidth at full width at half maximum, as shown in Fig. 2(b). The power intensity is normalized to the peak amplitude at the resonance frequency. The Q factor of every pixel is shown in Fig. 2(c); the Q-factors increase with frequency according to the relation: $Q \propto 2\pi L f_0/R_s$, where L is the inductance (3 μH) of the LC filters and R_s is the series resistance of the circuit when a TES is superconducting, which consists of the effective shunt resistance (~ 1 m Ω) and a parasitic resistance. R_s has a relatively constant value in each TES circuit. There is some scatter in the Q factor performance in Fig. 2(c), which is mainly due to the variation of the series resistance. The value of the series resistance ranges between 1.6 and 2.7 m Ω , as plotted in Fig. 2(d).

The bolometers are based on a Ti/Au (35/185 nm) bilayer with an area of 20 (Length) \times 80 (Width) μm^2 beside a squared Au structure of 125 \times 125 in area and 200 nm in thickness. Both are on a 195 \times 195 μm^2 Si₃N₄ membrane island, which is suspended from the Si substrate by four long (400 μm), narrow (2 μm) and thin (250 nm) Si₃N₄ legs. The normal resistance (R_N) is 150 ± 10 m Ω according to the resistance-temperature (RT) measurement of identical TESs from a witness chip taken from the same wafer. The critical temperature (T_c) of the TES is 127 ± 3 mK, which is derived by fitting the measured saturation power (P_{sat}) of the TESs at different bath temperatures. This value is fairly constant (with $\pm 2.5\%$ variation) over the array. The R_s is 2.2 ± 0.5 m Ω , and the common inductance is ≤ 3 nH from the VTT's measurement.³¹ The warm electronics used

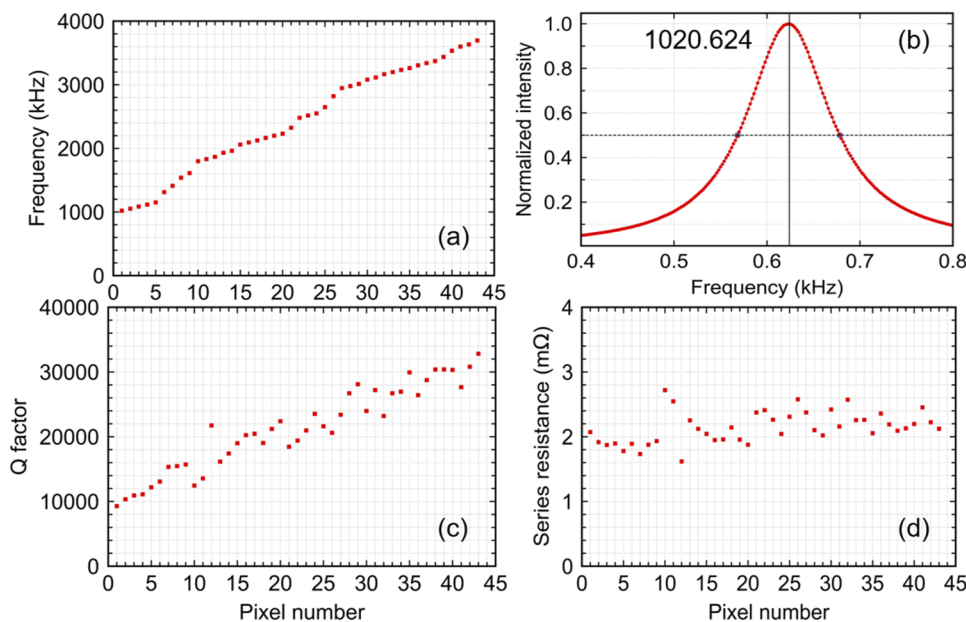


FIG. 2. (a) The resonance frequency of the LC filter for each TES in the superconducting state is plotted for different pixel numbers. (b) The measured resonance of pixel 1 used to determine the frequency and Q factor. The resonance frequency of pixel 1 is 1020.624 kHz. (c) The Q factor of all 43 resonators measured at 90 mK. (d) The series resistances of the circuit when each TES is superconducting for all the pixels.

are the same as in our previous publications.^{30,32} According to the thermal time constant $\tau = C/G$, where C is the heat capacity and G is the thermal conductance of the TES, the response time is proportional to C . Therefore, we decided to introduce an Au layer to replace the Tantalum (Ta) absorber in the previous TES array^{30,33} to increase the heat capacity, which is enlarged by a factor of 6.5.³⁴ In practice, we measured a decay time of such a TES of 20 ms when the TES was biased at 70% of R_{TES}/R_N in transition, while the decay time of the previous TES was 1 ms when it was at the same point in the transition.¹⁴ We measured a slow-down factor of 20, which is larger than the designed one (6.5) due to the fact that the effective time constant depends strongly also on the temperature sensitivity (α) of a TES. Although we have successfully slowed our TES down, the additional deposition of Au may affect the characteristics of the TES. For example, some pixels showed a wider superconducting-normal transition than what we usually observe. One reason could be the possible connection between deposited Au and superconducting TiAu bi-layer, which can affect the transition shape, thus cause a drop in α . Therefore, those pixels were excluded from our measurements, as mentioned earlier in the choice of pixels for measurement. We noticed additional structures around some Si_3N_4 legs, which could influence the value of G . The material of the additional structure is Si_3N_4 , presumably caused by insufficient etching.³⁵ The normal resistance of the previous TESs was 200 m Ω . Many TES could only be biased higher than 70% in transition, which made the TES resistance (R_{TES}) ≥ 140 m Ω . In the current array, all pixels can be biased lower than 50% in transition, which ensures $R_{TES} \leq 70$ m Ω (the normal resistance of TESs in the current array is ~ 150 m Ω). Therefore, the bias-current electric bandwidth of the TES, which is defined as $R_{TES}/2\pi L$ becomes at least a factor of 2 smaller than in the previous experiment since the R_{TES} is less than half of the previous value. For the slow TES, the bandwidth ratio ($Ratio_{bw}$) of the frequency spacing df_0 (32 kHz) and the electrical bandwidth (4 kHz) is 8, which is a factor of 2 higher than that of the previous TES. Since the carrier leakage between the neighbor pixels approximately equals $(R_{TES}/4\pi df_0 L)^2$, a factor of 2 increase in the $Ratio_{bw}$ will cause a factor of 2^2 decrease in the carrier leakage.^{4,14}

III. RESULTS AND DISCUSSIONS

A. Map of electrical cross talk

All 43 TES pixels in the array are biased in the transition at R_{TES}/R_n , which ranges between 10% and 50% at 90 mK. ECT results from the fact that part of the bias current from one detector couples to the other detectors. This can be due to three processes, namely carrier leakage, mutual inductance, and common inductance. The carrier leakage occurs when part of the current at a specific frequency that is intended for one detector leaks out to the other detectors because the LC filters are not ideal. The carrier leakage contributes typically from neighboring pixels in frequency, where the effect becomes larger if the pixel is closer, namely the adjacent pixels, and if the frequency space between two pixels is smaller. More detailed descriptions can be found in our previous publication.³⁰ By applying the ECT mapping technique described in Ref. 30, we generate an ECT map of 43 TESs, as shown in Fig. 3. We expect that the mutual inductance decreases significantly by using the microstrip wires instead of the coplanar wires. This is based on

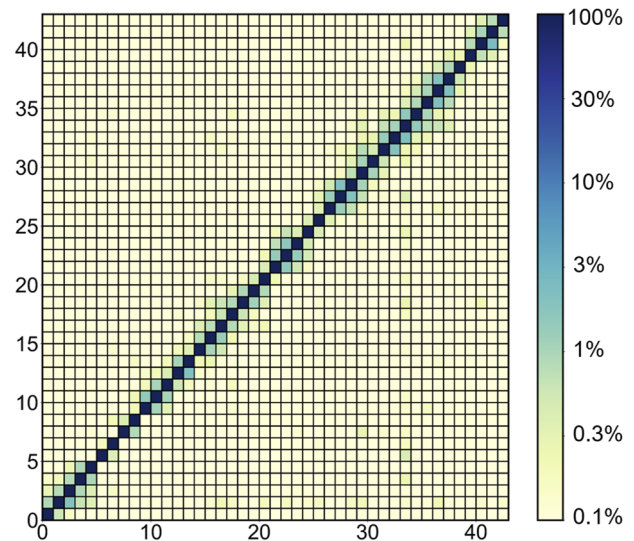


FIG. 3. Electrical cross talk (ECT) map of 43 pixels with a frequency spacing of 32 kHz. In this matrix, each row presents the ECT level of the pixels, caused by one of the pixels with dark blue color. The number represents the pixel from 1 to 43, which follows the order of the biasing voltage frequency from 1 to 3.5 MHz. The level of the ECT is indicated by color, quantified by the color bar in the figure. The column presents the ECT level of the pixels, which contributes the ECT to the pixel in dark blue (100%). ECT values of $<0.1\%$ are shown with the same color as 0.1% to make higher cross talk more visible in the map.

a simulation reported earlier,³⁶ where for a similar wiring geometry, the microstrip wires can reduce the mutual inductance by a factor of 43 in comparison with the coplanar wires. Here, we chose 24 Hz as our modulation frequency for ECT measurements since the thermal roll-off frequency of the TES bolometers is about 50 Hz and since there is low-frequency noise present below 10 Hz.

The ECT map is formed by a 43×43 matrix. In each row of the ECT map, the excited pixel number is the same as the row number with an ECT level of 100% (dark blue). The ECT levels observed in other pixels when this one is excited are indicated by the colors in that row. Similarly, in each column, the responding pixel number is the same as the column number and marked in dark blue. The ECT levels observed in this pixel when others are excited are indicated by the colors in that column. To highlight the pixels with an ECT larger than 1%, we plot the ECT values that are below 0.1% in the same color as 0.1%. In other words, in Fig. 3, we do not make a distinction for ECT values between 0% and 0.1%. We find 92.6% of the squares in the 43×43 ECT matrix to be light yellow, meaning that their ECT levels are below 0.1%, and some of them even approach zero (according to measured data, as low as 0.01%), although they are not visible because of the way we plot. Those 92.6% squares with less than 0.1% ECT are the pixels that are far away from the excited pixel in frequency space. Such a negligibly low ECT level is expected because the contribution from the mutual inductance should decrease significantly, for example, by an order of 40, by replacing the coplanar wires with the microstrip wires.³⁶ It is also because, in a carrier-leakage-dominated system, a factor of 2 increase in the frequency spacing will decrease the ECT by a factor of 4. We do observe the increased ECT levels from neighboring

pixels around the diagonal 100% line in Fig. 3. In detail, the squares correspond to adjacent pixels in frequency, contributing about 6.5% of the squares, show an ECT level between 0.1% and 1%. The ECT level between adjacent pixels is expected to vary between 0.4% and 0.7%³⁰ according to the difference in the bias points in transition. Therefore, the measured ECT matches well with the expected value. Therefore, this ECT map measurement confirms that our system is indeed dominated by carrier leakage.

We also find that there are about 0.9% of the squares show an ECT level higher than 1%. Those 0.9% of the squares correspond to the five pixels that have high carrier leakage (pixels 13, 29, 32–33, 41). One reason could be that those pixels have a narrower frequency spacing (i.e., 24 kHz) than the nominal frequency spacing of 32 kHz. Another reason could be that those pixels are not biased in a proper transition region, as will be discussed in Sec. III C.

B. Measurements of one pixel

If ECT levels are sufficiently low, there will be negligible differences in the measured characteristics and the performance of a TES between single-pixel mode (SPM) and multiplexing mode (MM). Before we show the results of all 43 pixels in the array, we first focus on presenting and analyzing the results of one pixel (pixel 1). The measured raw current–voltage (IV) curves of pixel 1 at 90 mK in single-pixel mode (red line) and multiplexing mode (blue line) are shown in Fig. 4(a). The difference between the two modes is negligible. By using the normal resistance measured from the witness chip and the current in the feedback circuit, the raw IV curve can be calibrated and is plotted in Fig. 4(b). The deviation between two IV curves becomes observable only when the TES is biased very low in transition ($\leq 5\%$) because the current leakage from neighbor pixels is comparable to its own current.¹⁴ Figure 4(c) shows the

observed saturation power (P_{sat}) at different bias points along with the bias-point on the transition R_{TES}/R_n , measured in both modes. P_{sat} is 44 fW in SPM and 46 fW in MM, respectively, where the difference of 2 fW corresponds to 4.5%, which is within the measurement uncertainty of 5% in IV measurements. Figure 4(d) shows the power fit to the P_{sat} data at different bath temperatures, measured in SPM, with the equation: $P_{bath} = K(T_c^n - T_{bath}^n)$. This equation describes the power flow from the TES to the bath, where K is a parameter scaling with the heat flux ($\approx 2.8 \times 10^{-11} \text{ W/K}^n$) and n a factor reflecting the characteristic of the thermal legs, which is found to be ≈ 3.0 for this pixel, within the expected range between 2 and 4. The G is found to be $1.5 \pm 0.1 \text{ pW/K}$, derived from the expression: $G = dP/dT = nKT_c^{n-1}$, where the T_c is $127 \pm 1 \text{ mK}$. Now, the phonon noise-limited NEP,¹ which is given by $\sqrt{4\gamma k_B G T_c^2}$ with $\gamma = 1$ and k_B the Boltzmann constant, is estimated to be $1.2 \pm 0.1 \text{ aW}/\sqrt{\text{Hz}}$.

We further study the noise performance of pixel 1, which is biased at 20% of R_{TES}/R_n , as plotted in Fig. 5(a). The read-out noise level is $15.5 \text{ pA}/\sqrt{\text{Hz}}$, as shown by the green line in the plot. The measured current noise in black matches very well with the simulated current noise (red). The simulated current noise includes phonon noise (in blue), Johnson noise (orange), and read-out noise (green). The phonon noise is calculated with the parameters extracted from the measurements in Fig. 4 (i.e., G , T_c) and the impedance measurement.³⁷ From the impedance measurement of this pixel, we derive α to be 205, and β to be 1.7 at the operating point. Below the detector roll-off frequency (50 Hz), the phonon noise of the blue line contributes mostly to the red line, suggesting that the TES bolometer is phonon-noise dominated in the relevant frequency range. The deviation between the simulated and measured noise occurs at frequencies below 10 Hz, which is probably due to excess noise and 1/f noise. We also noticed that the measured noise

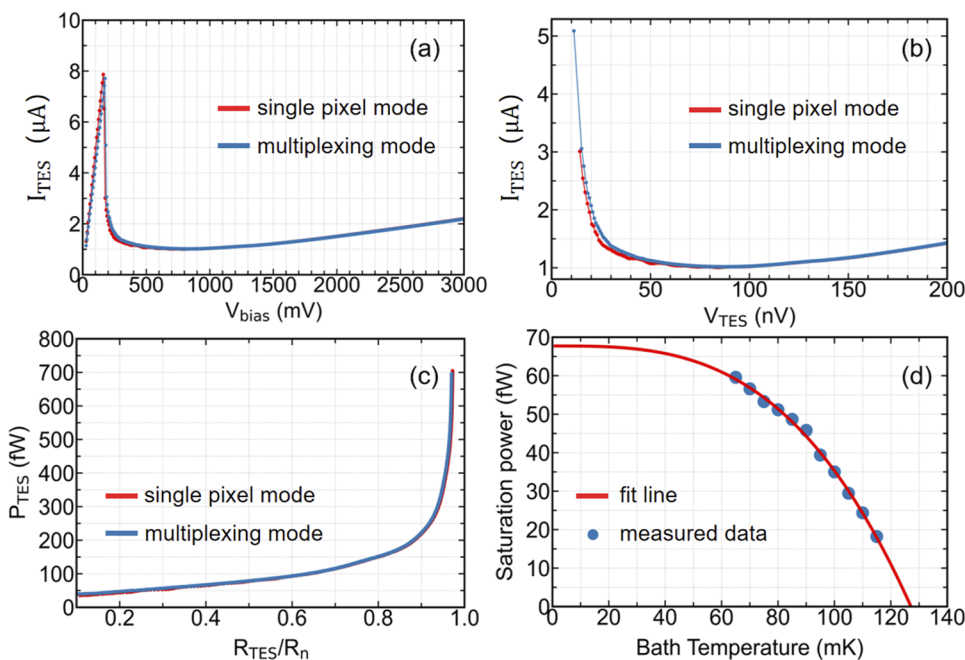


FIG. 4. (a) Measured raw IV curve of pixel 1, where the red line indicates data measured in single-pixel mode and the blue line represents the data measured in multiplexing mode. (b) Calibrated IV from the raw data. (c) PR curve of this pixel. (d) A power-law fit of measured saturation power as a function of bath temperature. The fitted T_c is 127 mK.

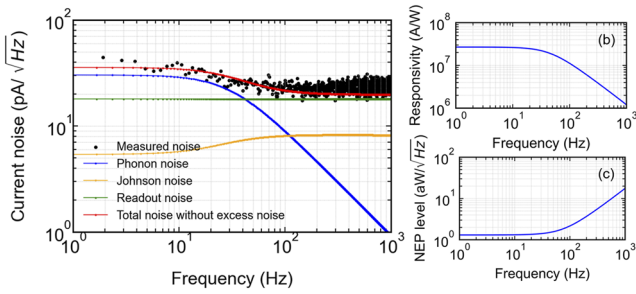


FIG. 5. (a) Plot of the measured current noise of pixel 1 at 20% in transition and the expected noise according to the parameters derived from an impedance measurement. The expected and measured current noise levels match well except for the low-frequency range (<10 Hz); (b) Calculated responsivity of this pixel. (c) NEP calculated with expected noise and responsivity. The NEP is $1.3 \text{ aW}/\sqrt{\text{Hz}}$.

at the high end of frequency is slightly higher than the simulated total noise. The difference is probably due to the higher readout noise caused by a different SQUID setting. It could also be an underestimation of Johnson noise from the load resistor. Figure 5(b) shows the responsivity of this pixel with a value of $2.5 \times 10^7 \text{ A/W}$. Figure 5(c) shows the estimated NEP of $1.3 \text{ aW}/\sqrt{\text{Hz}}$ from the simulated noise, which is the same as the phonon noise dominated NEP, estimated from G and T_c .

C. Measurements of 43 pixels

Now we turn to the performance of the 43 TES bolometers in SPM and MM. As shown in Fig. 6(a), all the detectors are biased in the range between 10% and 50% in transition. Compared to the measurements using the previous TES, which are relatively fast,^{14,38} now we are able to bias all detectors below 50% in transition without any

unwanted oscillations. To increase the signal-to-noise ratio (SNR) in the readout circuit as well as to minimize the carrier leakage, it is preferred to bias our TES as low as possible in transition. However, some TES detectors have undesirable structures (not smooth) when they are biased low in the transition. Therefore, we choose an appropriate bias point where the transition is low and the IV curve is smooth as well. Most pixels behave normally when they are biased between 10% and 50% in transition. However, as we noticed from the ECT map, five pixels are likely not biased in a stable operating position on the transition. Figure 6(b) shows the TES voltage for each TES when it is biased at the usual operating point. To calculate the NEP, we, in principle, need to calculate the current noise divided by the responsivity as expressed by Eq. (1),

$$NEP_{measured} = \frac{\sqrt{S_{I,measured}^2 - S_{I,read}^2}}{s_{AC}}, \quad (1)$$

where $NEP_{measured}$ is the NEP derived from experiment, $S_{I,measured}^2$ is the measured current noise, $S_{I,read}^2$ is the readout noise, and s_{AC} is the responsivity of the TES. The can be expressed as¹

$$s_{AC} = -\frac{1}{V_{TES}} \left(\frac{L}{\tau_{ele} R_{TES} \mathcal{L}} + \left(1 - \frac{R_s}{R_{TES}} \right) + i2\pi f \frac{L\tau}{R_{TES} \mathcal{L}} \left(\frac{1 - \mathcal{L}}{\tau} + \frac{1}{\tau_{ele}} \right) - \frac{(2\pi f)^2 \tau}{\mathcal{L}} \frac{L}{R_{TES}} \right)^{-1}, \quad (2)$$

where τ_{ele} is the electrical response time that can be represented by $\frac{L}{R_s + R_{TES}(1+\beta)}$ with \mathcal{L} being the loop gain, and f is the signal frequency. Since we are only interested in the frequency range lower than 50 Hz and $R_s \ll R_{TES}$, Eq. (2) can be simplified to

$$s_{AC} = -\frac{1}{V_{TES}} \left(\frac{1+\beta}{\mathcal{L}} + 1 \right)^{-1}. \quad (3)$$

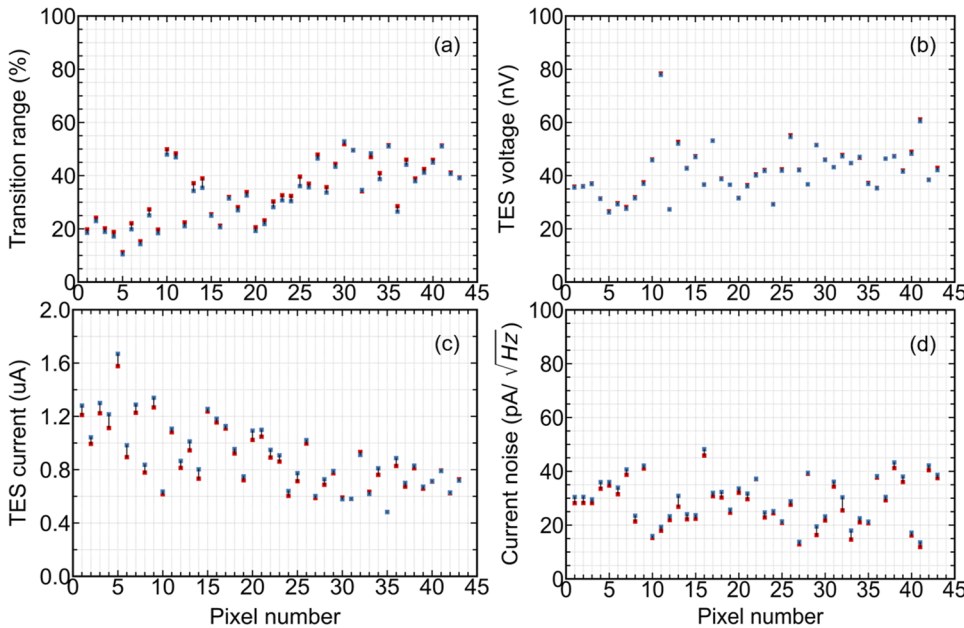


FIG. 6. (a) An operating transition range of 43 pixels in SM (red squares) and MM (blue squares). Each pixel has the same bias voltage in both modes. In MM, the transition is slightly lower due to cross talk, although they are very close. (b) The voltage of each TES in both modes. (c) The current of each TES in both modes. The current is slightly higher in MM because it is slightly lower in transition. (d) The current noise of each pixel in both modes. Similar to TES current, the current noise is higher in MM due to the TES being lower in transition.

In practice, the loop gain \mathcal{L} is much larger than 1, so we use V_{TES} and replace $\frac{1}{s_{AC}}$ to derive the $NEP_{measured}$ by

$$NEP_{measured} = V_{TES} \times \sqrt{S_{I,measured}^2 - S_{I,read}^2} \quad (4)$$

Figure 6(c) plots the TES current of each pixel in both SPM and MM. The tendency of the decrease in the TES current corresponds to the tendency of the increase in the transition range in Fig. 6(a), since the TES current becomes larger when a TES is biased lower in transition. We also notice that the difference in TES current between two modes becomes larger when a TES is biased lower in transition, which is due to the fact that the detector is more sensitive to current change there. The measured current noise of each pixel in both modes is shown in Fig. 6(d). Most of the current noise values are between 20 and 40 pA/ $\sqrt{\text{Hz}}$, which is close to the expected phonon noise values of our TESs, corresponding to the operating region of the transition. Although most pixels show the same values in SPM and MM within the measurement error, five of them (pixels 13, 29, 32–33, and 41) show a relatively large difference (>10%) between the two modes. Those are actually the pixels with a relatively high carrier leakage.

P_{sat} is calculated from the calibrated IV curve of each pixel at 90 mK. The NEP and P_{sat} of all 43 pixels, biased in the frequency range from 1 to 3.5 MHz, measured in both SPM and MM, are shown in Figs. 7 and 8, respectively. We found the NEPs to be

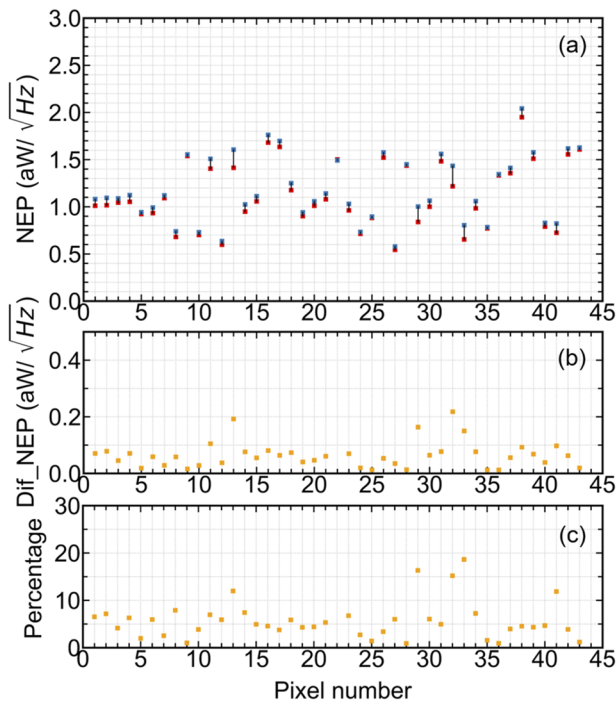


FIG. 7. (a) A measured NEP of 43 pixels in SM (red squares) and MM (blue squares). Most NEPs are scattered around 1.2 aW/ $\sqrt{\text{Hz}}$, but the value is the same in both modes. (b) Difference between the NEPs in two modes. (c) Differences in NEP in percentage between SM and MM, derived from (b) with respect to the NEP in MM; only five pixels show a difference greater than 10% because of the high ECT level (>1%).

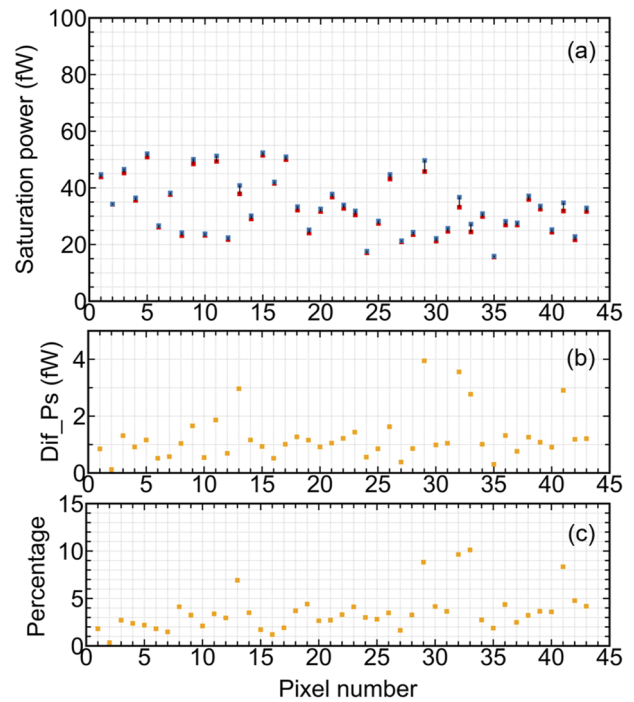


FIG. 8. (a) Measured saturation power of 43 pixels in the two modes. The P_{sat} value of each pixel is taken at 20% in the transition. Most saturation powers are scattered around 35 fW, and the values are the same in both modes. (b) The differences of P_{sat} are measured in the two modes. (c) The percentage difference in P_{sat} between SM and MM, derived from (b) with respect to P_{sat} in MM; only five pixels show a difference greater than 5% because of the high ECT level (>1%).

between 0.6 and 1.8 aW/ $\sqrt{\text{Hz}}$ over the 43 pixels, with a mean value of 1.2 aW/ $\sqrt{\text{Hz}}$, while the P_{sat} varies from 20 to 50 fW, with a mean value of 35 fW. Both the measured NEP and P_{sat} of most pixels are the same in either SPM or MM, which is consistent with the cross talk measurement described in Sec. III A.

Compared to the previous TES array used in Refs. 14 and 30, which was fabricated with a wet-etching process, the uniformity of the Si_3N_4 legs and thus the G should be improved for the TES bolometers in this array because of the use of Deep Reactive Ion Etching (DRIE). However, G still has a relatively large scatter (up to a factor of 9). The reason could be remaining structures on some of the Si_3N_4 legs in some TES, as shown in Fig. 1(b). Another source of the non-uniformity could be the introduction of the Au structure in our TES. It is generally known that TESs can be sensitive to any changes in the fabrication. The variations in measured G cannot be due to stray light because of the absence of absorbers or to cross talk because the level is extremely low (<1%). Furthermore, any influence from the readout system can be excluded since the scattering is not frequency-dependent.

IV. CONCLUSIONS

In conclusion, we succeeded in increasing the response time of our TES by a factor of 20 by adding an Au structure to the TES, achieving an effective time constant of 20 ms at a transition bias

point of 70% for R_{TES}/R_N . Therefore, we not only have a much larger bandwidth ratio (frequency spacing/electrical bandwidth) of 8, but also allow the TES to be biased low in the transition without oscillations. We have mapped the electrical cross talk of 43 pixels in an array with a nominal frequency spacing of 32 kHz. We have found that 38 pixels show an electrical cross talk level of less than 1%, which is dominated by the carrier leakage. Reduced cross talk is attributed to the use of microstrip wiring in the array, which minimizes the mutual inductance. We also observed five pixels with a cross talk level higher than 1% due to the reduced frequency spacing and structure in the IV curves. Our study suggests that our FDM can have a low enough ECT level to satisfy the requirement for a space instrument such as SPICA/SAFARI. We have read out 43 pixels simultaneously in the frequency range 1–3.5 MHz, with an NEP level ranging from 0.6 to 1.8 aW/ $\sqrt{\text{Hz}}$ and a saturation power varying between 20 and 50 fW. All the pixels show the same results in single-pixel mode and multiplexing mode except for the five pixels with a high cross talk level. The measured noise spectrum is in good agreement with the simulated noise based on measured parameters from an impedance measurement, confirming that our TES is dominated by phonon noise. That 43 pixels were chosen out of the half array (88-pixel) for our experiment is unfortunately due to the nonuniformity of the available TES batch. In the future, with a more uniform TES bolometer array and a larger readout bandwidth (up to 5 MHz), we can foresee our FDM reading out 130 pixels in one SQUID readout channel.

Practical FIR TES bolometers require an absorber. So, we need to introduce the Ta absorber together with a metal structure with a higher heat capacity. Palladium-gold (PdAu), as suggested by Ref. 39, or Pd, as suggested by Ref. 40 can be patterned next to the absorber on the detector. A detailed layout should be optimized for a specific application. Pd is, in particular, attractive for this application because its heat capacity is 11 times higher than Au.⁴¹ Furthermore, one can also explore non-superconducting thin films as absorbers instead of the superconducting Ta to increase the heat capacity and thus the thermal response time.

ACKNOWLEDGMENTS

We acknowledge M. Kiviranta at VTT for providing the two-stage SQUIDs and E. Taralli and K. Ravensberg for running the ADR cooler. This work benefits greatly from the knowledge and existing hardware from a long development history of the FDM technology contributed by many people at SRON, including S. Ilyas, R. Hijmering, R. den Hartog, L. Gottardi, H. Akamatsu, D. Vaccaro, B. Jackson, P. de Korte, D. Boersma, B. van Leeuwen, and J. Nieuwenhuizen. Q. Wang also thanks J. G. bij de Vaate for supporting his Ph.D. activity within the Instrument Science Group at SRON. Q. Wang is funded partly by the China Scholarship Council (CSC) Grant No. 201706030152 and partly by the University of Groningen.

AUTHOR DECLARATIONS

Conflict of Interest

The authors have no conflicts to disclose.

Author Contributions

Q. Wang: Conceptualization (equal); Data curation (equal); Investigation (equal); Methodology (equal); Software (equal); Writing – original draft (equal); Writing – review & editing (equal). **P. Khosropanah:** Data curation (equal); Formal analysis (equal); Methodology (equal); Supervision (equal); Writing – original draft (equal); Writing – review & editing (equal). **J. van der Kuur:** Data curation (equal); Formal analysis (equal); Methodology (equal); Writing – review & editing (equal). **G. de Lange:** Funding acquisition (equal); Project administration (equal); Supervision (equal); Writing – review & editing (equal). **M. D. Audley:** Methodology (equal); Software (equal); Writing – review & editing (equal). **A. Aminaei:** Data curation (supporting); Methodology (supporting); Writing – review & editing (supporting). **S. Ilyas:** Investigation (equal); Methodology (equal); Resources (equal). **M. L. Ridder:** Methodology (supporting); Resources (supporting); Writing – review & editing (supporting). **A. J. van der Linden:** Resources (supporting); Writing – review & editing (supporting). **M. P. Bruijn:** Methodology (supporting); Resources (supporting). **F. van der Tak:** Supervision (supporting); Writing – review & editing (supporting). **J. R. Gao:** Conceptualization (equal); Supervision (equal); Writing – original draft (equal); Writing – review & editing (equal).

DATA AVAILABILITY

The data that support the findings of this study are available from the corresponding author upon reasonable request.

REFERENCES

- 1 K. D. Irwin and G. C. Hilton, *Transition-Edge Sensors* (Springer, Berlin, Heidelberg, 2005), pp. 63–150.
- 2 D. Farrah, K. E. Smith, D. Ardila, C. M. Bradford, M. J. Dipirro, C. Ferkinhoff, J. Glenn, P. F. Goldsmith, D. T. Leisawitz, T. Nikola, N. Rangwala, S. A. Rinehart, J. G. Staguhn, M. Zemcov, J. Zmuidzinas, J. Bartlett, S. J. Carey, W. J. Fischer, J. R. Kamenetzky, J. Kartaltepe, M. D. Lacy, D. C. Lis, L. S. Locke, E. Lopez-Rodriguez, M. MacGregor, E. Mills, S. H. Moseley, E. J. Murphy, A. Rhodes, M. J. Richter, D. Rigopoulou, D. B. Sanders, R. Sankrit, G. Savini, J.-D. Smith, and S. Stierwalt, *J. Astron. Telesc. Instrum. Syst.* **5**, 020901 (2019).
- 3 T. M. Lanting, H.-M. Cho, J. Clarke, W. L. Holzapfel, A. T. Lee, M. Lueker, P. L. Richards, M. A. Dobbs, H. Spieler, and A. Smith, *Appl. Phys. Lett.* **86**, 112511 (2005).
- 4 M. A. Dobbs, M. Lueker, K. A. Aird, A. N. Bender, B. A. Benson, L. E. Bleem, J. E. Carlstrom, C. L. Chang, H.-M. Cho, J. Clarke, T. M. Crawford, A. T. Crites, D. I. Flanigan, T. de Haan, E. M. George, N. W. Halverson, W. L. Holzapfel, J. D. Hrubes, B. R. Johnson *et al.*, *Rev. Sci. Instrum.* **83**, 073113 (2012).
- 5 B. D. Jackson, P. A. J. de Korte, J. van der Kuur, P. D. Mauskopf, J. Beyer, M. P. Bruijn, A. Cros, J. Gao, D. Griffin, R. den Hartog, M. Kiviranta, G. de Lange, B. van Leeuwen, C. Macculli, L. Ravera, N. Trappe, H. van Weers, and S. Withington, *IEEE Trans. Terahertz Sci. Technol.* **2**, 12 (2012).
- 6 R. den Hartog, J. Beyer, D. Boersma, M. Bruijn, L. Gottardi, H. Hoevers, R. Hou, M. Kiviranta, P. de Korte, J. van der Kuur, B.-J. van Leeuwen, M. Lindeman, and A. Nieuwenhuizen, *IEEE Trans. Appl. Supercond.* **21**, 289–293 (2011).
- 7 K. D. Irwin, L. R. Vale, N. E. Bergren, S. Deiker, E. N. Grossman, G. C. Hilton, S. W. Nam, C. D. Reintsema, D. A. Rudman, and M. E. Huber, *AIP Conf. Proc.* **605**, 301–304 (2002).
- 8 W. B. Doriese, J. A. Beall, S. Deiker, W. D. Duncan, L. Ferreira, G. C. Hilton, K. D. Irwin, C. D. Reintsema, J. N. Ullom, L. R. Vale, and Y. Xu, *Appl. Phys. Lett.* **85**, 4762–4764 (2004).
- 9 D. Prêle, F. Voisin, M. Piat, T. Decourcelle, C. Perbost, C. Chapron, D. Rambaud, S. Maestre, W. Marty, and L. Montier, *J. Low Temp. Phys.* **184**, 363–368 (2016).

- ¹⁰K. D. Irwin and K. W. Lehnert, *Appl. Phys. Lett.* **85**, 2107–2109 (2004).
- ¹¹J. A. B. Mates, G. C. Hilton, K. D. Irwin, L. R. Vale, and K. W. Lehnert, *Appl. Phys. Lett.* **92**, 023514 (2008).
- ¹²Y. Nakashima, F. Hirayama, S. Kohjiro, H. Yamamori, S. Nagasawa, A. Sato, S. Yamada, R. Hayakawa, N. Y. Yamasaki, K. Mitsuda, K. Nagayoshi, H. Akamatsu, L. Gottardi, E. Taralli, M. P. Bruijn, M. L. Ridder, J. R. Gao, and J. W. A. den Herder, *Appl. Phys. Lett.* **117**, 122601 (2020).
- ¹³H. Akamatsu, D. Vaccaro, L. Gottardi, J. van der Kuur, C. P. de Vries, M. Kiviranta, K. Ravensberg, M. D'Andrea, E. Taralli, M. de Wit, M. P. Bruijn, P. van der Hulst, R. H. den Hartog, B.-J. van Leeuwen, A. J. van der Linden, A. J. McCalden, K. Nagayoshi, A. C. T. Nieuwenhuizen, M. L. Ridder, S. Visser, P. van Winden, J. R. Gao, R. W. M. Hoogeveen, B. D. Jackson, and J.-W. A. den Herder, *Appl. Phys. Lett.* **119**, 182601 (2021).
- ¹⁴Q. Wang, P. Khosropanah, J. van der Kuur, G. de Lange, M. D. Audley, A. Aminaei, M. L. Ridder, A. J. van der Linden, M. P. Bruijn, F. van der Tak, and J. R. Gao, *Appl. Phys. Lett.* **119**, 182602 (2021).
- ¹⁵D. Schwan, P. A. R. Ade, K. Basu, A. N. Bender, F. Bertoldi, H.-M. Cho, G. Chon, J. Clarke, M. Dobbs, D. Ferrusca, R. Güsten, N. W. Halverson, W. L. Holzappel, C. Horellou, D. Johansson, B. R. Johnson, J. Kennedy, Z. Kermish, R. Kneissl, T. Lanting, A. T. Lee, M. Lueker, J. Mehl, K. M. Menten, D. Muders, F. Pacaud, T. Plagge, C. L. Reichardt, P. L. Richards, P. Schaaf, P. Schilke, M. W. Sommer, H. Spieler, C. Tucker, A. Weiss, B. Westbrook, and O. Zahn, *Rev. Sci. Instrum.* **82**, 091301 (2011).
- ¹⁶J. Montgomery, A. J. Anderson, J. S. Avva, A. N. Bender, M. A. Dobbs, D. Dutcher, T. Elleflot, A. Foster, J. C. Groh, W. L. Holzappel, D. Howe, N. Huang, A. E. Lowitz, G. I. Noble, Z. Pan, A. Rahlin, D. Riebel, G. Smecher, A. Suzuki, and N. Whitehorn, *Proc. SPIE* **11453**, 114530X (2020).
- ¹⁷H. Logan, Ph.D. thesis, University of California, San Diego, 2019.
- ¹⁸M. Abitbol, A. M. Aboobaker, P. Ade, D. Araujo, F. Aubin, C. Baccigalupi, C. Y. Bao, D. Chapman, J. Didier, M. Dobbs, S. M. Feeney, C. Geach, W. Grainger, S. Hanany, K. Helson, S. Hillbrand, G. Hilton, J. Hubmayr, K. Irwin, A. Jaffe, B. Johnson, T. Jones, J. Klein, A. Korotkov, A. Lee, L. Levinson, M. Limon, K. MacDermid, A. D. Miller, M. Milligan, K. Raach, B. R. Kjennerud, C. Reintsema, I. Sagiv, G. Smecher, G. S. Tucker, B. Westbrook, K. Young, and K. Zilic, *Astrophys. J., Suppl. Ser.* **239**, 8 (2018).
- ¹⁹K. MacDermid, A. M. Aboobaker, P. Ade, F. Aubin, C. Baccigalupi, C. Bandura, C. Bao, J. Borrill, D. Chapman, J. Didier, M. Dobbs, J. Grain, W. Grainger, S. Hanany, K. Helson, S. Hillbrand, G. Hilton, H. Hubmayr, K. Irwin, B. Johnson, A. Jaffe, T. Jones, T. Kisner, J. Klein, A. Korotkov, A. Lee, L. Levinson, M. Limon, A. Miller, M. Milligan, E. Pascale, K. Raach, B. Reichborn-Kjennerud, C. Reintsema, I. Sagiv, G. Smecher, R. Stompor, M. Tristram, G. Tucker, B. Westbrook, and K. Zilic, *Proc. SPIE* **9153**, 915311 (2014).
- ²⁰A. Tartari, A. M. Baldini, F. Cei, L. Galli, M. Grassi, D. Nicolò, M. Piendibene, F. Spinella, D. Vaccaro, and G. Signorelli, *J. Low Temp. Phys.* **199**, 212 (2020).
- ²¹The LSPE Collaboration, G. Addamo, P. A. R. Ade, C. Baccigalupi, A. M. Baldini, P. M. Battaglia, E. S. Battistelli, A. Baù, P. de Bernardis, M. Bersanelli, M. Biasotti, A. Boscaleri, B. Caccianiga, S. Caprioli, F. Cavaliere, F. Cei, K. A. Cleary, F. Columbro, G. Coppi, A. Coppolecchia, F. Cuttaia, G. D'Alessandro, G. De Gasperis, M. De Petris, V. Fafone, F. Farsian, L. Ferrari Barusso, F. Fontanelli, C. Franceschet, T. C. Gaier, L. Galli, F. Gatti, R. Genova-Santos, M. Gerbino, M. Gervasi, T. Ghigna, D. Grosso, A. Gruppuso, R. Gualtieri, F. Incardona, M. E. Jones, P. Kangaslanti, N. Krachmalnicoff, L. Lamagna, M. Lattanzi, C. H. López-Caraballo, M. Lumia, R. Mainini, D. Maino, S. Mandelli, M. Maris, S. Masi, S. Matarrese, A. May, L. Mele, P. Mena, A. Mellena, R. Molina, D. Molinari, G. Morgante, U. Natale, F. Nati, P. Natoli, L. Pagano, A. Paiella, F. Panico, F. Paonessa, S. Paradiso, A. Passerini, M. Perez-de-Taoro, O. A. Peverini, F. Pezzotta, F. Piacentini, L. Piccirillo, G. Pisano, G. Polenta, D. Poletti, G. Presta, S. Realini, N. Reyes, A. Rocchi, J. A. Rubino-Martin, M. Sandri, S. Sartor, A. Schillaci, G. Signorelli, B. Siri, M. Soria, F. Spinella, V. Tapia, A. Tartari, A. C. Taylor, L. Terenzi, M. Tomasi, E. Tommasi, C. Tucker, D. Vaccaro, D. M. Viganò, F. Villa, G. Virone, N. Vittorio, A. Volpe, R. E. J. Watkins, A. Zacchei, and M. Zannoni, *J. Cosmol. Astropart. Phys.* **2021**, 008.
- ²²M. Hazumi, P. A. R. Ade, Y. Akiba, D. Alonso, K. Arnold, J. Aumont *et al.*, *J. Low Temp. Phys.* **194**, 443–452 (2019).
- ²³G. C. Jaehnig, K. Arnold, J. Austermann, D. Becker, S. Duff, N. W. Halverson, M. Hazumi, G. Hilton, J. Hubmayr, A. T. Lee, M. Link, A. Suzuki, M. Vissers, S. Walker, and B. Westbrook, *J. Low Temp. Phys.* **199**, 646 (2020).
- ²⁴P. R. Roelfsema, H. Shibai, L. Armus, D. Arrazola, M. Audard, M. D. Audley, C. M. Bradford, I. Charles, P. Dieleman, Y. Doi, L. Duband, M. Eggers, J. Evers, I. Funaki, J. R. Gao, M. Giard, A. di Giorgio, L. M. G. Fernández, M. Griffin, F. P. Helmich, R. Hijmering, R. Huisman, D. Ishihara, N. Isobe, B. Jackson, H. Jacobs, W. Jellema, I. Kamp, H. Kaneda, M. Kawada, F. Kemper, F. Kerschbaum, P. Khosropanah, K. Kohnno, P. P. Kooijman, O. Krause, J. van der Kuur, J. Kwon, W. M. Laauwen, G. de Lange, B. Larsson, D. van Loon, S. C. Madden, H. Matsuhara, F. Najarro, T. Nakagawa, D. Naylor, H. Ogawa, T. Onaka, S. Oyabu, A. Poglitsch, V. Reveret, L. Rodriguez, L. Spinoglio, I. Sakon, Y. Sato, K. Shinozaki, R. Shipman, H. Sugita, T. Suzuki, F. F. S. van der Tak, J. T. Redondo, T. Wada, S. Y. Wang, C. K. Wafelbakker, H. van Weers, S. Withington, B. Vandenbussche, T. Yamada, and I. Yamamura, *Publ. Astron. Soc. Aust.* **35**, e030 (2018).
- ²⁵M. D. Audley, G. de Lange, J. R. Gao, B. D. Jackson, R. A. Hijmering, M. L. Ridder, M. P. Bruijn, P. R. Roelfsema, P. A. R. Ade, S. Withington, C. M. Bradford, and N. A. Trappe, *Proc. SPIE* **10708**, 107080K (2018).
- ²⁶L. Gottardi and K. Nagayoshi, *Appl. Sci.* **11**, 3793 (2021).
- ²⁷M. L. Ridder, P. Khosropanah, R. A. Hijmering, T. Suzuki, M. P. Bruijn, H. F. C. Hoeyers, J. R. Gao, and M. R. Zuiddam, *J. Low Temp. Phys.* **184**, 60 (2016).
- ²⁸T. Suzuki, P. Khosropanah, M. L. Ridder, R. A. Hijmering, J. R. Gao, H. Akamatsu, L. Gottardi, J. van der Kuur, and B. D. Jackson, *J. Low Temp. Phys.* **184**, 52–59 (2016).
- ²⁹M. Kiviranta, L. Grönberg, and H. Sipola, *Supercond. Sci. Technol.* **24**, 049501 (2011).
- ³⁰Q. Wang, P. Khosropanah, J. van der Kuur, G. de Lange, M. D. Audley, A. Aminaei, R. Hijmering, M. L. Ridder, S. Ilyas, A. J. van der Linden, M. P. Bruijn, F. van der Tak, and J. R. Gao, *Rev. Sci. Instrum.* **92**, 014710 (2021).
- ³¹M. Kiviranta, "SQUID development: current status" (unpublished, 2018).
- ³²Q. Wang, M. D. Audley, P. Khosropanah, J. van der Kuur, G. de Lange, A. Aminaei, D. Boersma, F. van der Tak, and J.-R. Gao, *J. Low Temp. Phys.* **199**, 817 (2020).
- ³³The deposition of the Au layer was done using Electron Beam deposition in combination with a lift-off process. We use AZ-5214 image reversal photoresist for pattern definition and deposit first a 3 nm Titanium (Ti) layer for adhesion followed by 200 nm Au. The gap between TES bilayer structure and the Au structure is 10 μm .
- ³⁴The nominal parameter of C/V (heat capacity/volume) is 7 J/(K). The previous heat capacity is 4 fJ/K m^3 in our bolometers. After adding a 200 nm thick Au structure with an area of $125 \times 125 \mu\text{m}^2$, the heat capacity in our current bolometers becomes 26 fJ/K. Therefore, the heat capacity increases by a factor of 6.5.
- ³⁵The etching of Si_3N_4 legs are performed from the front side of the detector wafer, which takes usually 5 min. However, for this particular wafer, even we performed an 8 min, longer etching, there are still some Si_3N_4 structures left in the legs. The cause is unclear.
- ³⁶X. Yan, M. P. Bruijn, H. J. van Weers, R. A. Hijmering, J. van der Kuur, and J. R. Gao, *IEEE Trans. Appl. Supercond.* **25**, 2100105 (2015).
- ³⁷E. Taralli, P. Khosropanah, L. Gottardi, K. Nagayoshi, M. L. Ridder, M. P. Bruijn, and J. R. Gao, *AIP Adv.* **9**, 045324 (2019).
- ³⁸R. Hijmering, R. den Hartog, M. Ridder, A. van der Linden, J. van der Kuur, J. R. Gao, and B. Jackson, *Proc SPIE* **9914**, 99141C (2016).
- ³⁹E. M. George, J. E. Austermann, J. A. Beall, D. Becker, B. A. Benson, L. E. Bleem, J. E. Carlstrom, C. L. Chang, H.-M. Cho, A. T. Crites, M. A. Dobbs, W. Everett, N. W. Halverson, J. W. Henning, G. C. Hilton, W. L. Holzappel, J. Hubmayr, K. D. Irwin, D. Li, M. Lueker, J. J. McMahon, J. Mehl, J. Montgomery, T. Natoli, J. P. Nibarger, M. D. Niemack, V. Novosad, J. E. Ruhl, J. T. Sayre, E. Shirokoff, K. T. Story, G. Wang, V. Yefremenko, K. W. Yoon, and E. Young, *J. Low Temp. Phys.* **176**, 383–391 (2014).
- ⁴⁰K. Rostem, D. T. Chuss, F. A. Colazo, E. J. Crowe, K. L. Denis, N. P. Lourie, S. H. Moseley, T. R. Stevenson, and E. J. Wollack, *J. Appl. Phys.* **115**, 124508 (2014).
- ⁴¹P. M. Laufer and D. A. Papaconstantopoulos, *Phys. Rev. B* **35**, 9019 (1987).